PHYSICAL REVIEW MATERIALS **6**, 043604 (2022)

Angular-dependent interatomic potential for large-scale atomistic simulation of the Fe-Cr-H ternary system

Sergei Starikov,[1,*] Daria Smirnova,[2] Tapaswani Pradhan,[1] Ilia Gordeev,[3] Ralf Drautz,[1] and Matous Mrovec[1]
[1]*The Interdisciplinary Centre for Advanced Materials Simulation (ICAMS), Ruhr-Universität Bochum, Germany*
[2]*Computational Materials Design, Max-Planck-Institut für Eisenforschung GmbH, Düsseldorf, Germany*
[3]*Joint Institute for High Temperatures of RAS, Moscow, Russia*

(Received 7 March 2022; accepted 12 April 2022; published 26 April 2022)

The recently developed angular-dependent potential for pure iron was advanced to the interatomic potential of the Fe-Cr-H ternary system. The new potential allows to simulate Fe-Cr alloys for a wide range of compositions and different concentrations of hydrogen. The angular-dependent format of the model and the development procedure based on the machine learning approach allow to achieve a favorable balance between the computation cost and the reliability of the created parametrization. As part of potential validation, we performed a large number of tests of both the binary metallic alloys and hydrogen interactions. The applicability of the potential is demonstrated by large-scale simulations of hydrogen diffusion in the vicinity of crystal defects.

DOI: 10.1103/PhysRevMaterials.6.043604

I. INTRODUCTION

Fe-Cr alloy is a basis for one of the most important structural materials—stainless steel. The resistance to corrosion and low maintenance make stainless steel suitable for various industrial applications where both the strength and the resistance to environmental degradation are required. An increased use of stainless steels is also expected in the growing hydrogen industry, where specific requirements are imposed on the materials for hydrogen storage and transport. One of the most critical issues in H-related applications is the resistance against hydrogen embrittlement (HE) [1,2]. However, absence of full understanding of HE mechanisms in complex multicomponent alloys hinders their broader application due to safety concerns. Currently, data on the relation between composition, temperature, strain conditions, and HE propensity are obtained mostly empirically and require extensive experimental testing and validation.

In this work, we developed an angular-dependent interatomic potential (ADP) for the ternary Fe-Cr-H system that enables to carry out large-scale atomistic simulations of HE-related phenomena for a broad range of Fe-Cr alloys. The model is based on our recent ADP parametrization for pure iron [3] which was shown to give a good overall description of both structures and energetics of various crystal defects. The new ternary model was developed using the same procedure that utilizes a large database of reference quantum-mechanical data and a machine learning (ML) fitting approach. The combination of ML interpolation and physics-based functional forms of ADP provides an optimal balance between the computation cost and the reliability of the model.

The paper is organized as follows: Existing interatomic potentials for the binary Fe-Cr and Fe-H systems are reviewed in Sec. II. In Sec. III, the construction of the ADP parametrization for the ternary Fe-Cr-H system is described in detail. Sections IV and V present an extensive validation of the developed model for both the elemental and binary systems. In Sec. VI, we apply the model to evaluate various diffusion phenomena using large-scale atomistic simulations. Section VII provides a summary and conclusions.

II. INTERATOMIC POTENTIALS FOR THE FE-CR AND FE-H SYSTEMS

To our knowledge, there exist classical interatomic potentials for the binary Fe-Cr and Fe-H systems, but no interatomic potential for the ternary Fe-Cr-H system is available. A comprehensive overview of various Fe potentials may be found in our recent study [3]. Here we briefly review only the binary potentials.

A. Fe-Cr potentials

There are many classical interatomic potentials aimed at the simulation of stainless steel [4–10]. These models describe atomic interaction in the Fe-Cr system based on either the embedded atom method (EAM) [11] or the modified embedded atom method (MEAM) [12]. Commonly, the models incorporate already existing parametrizations for pure elements and complement them with the parametrization of the Fe-Cr interaction only. The main focus is usually given to the anomalous dependence of the mixing enthalpy on Cr concentration [13–15] and to point defect properties. A variety of validation tests of these models covering fundamental material properties can be found in the NIST Repository of Interatomic Potentials [16,17] and the OpenKIM Knowledgebase of Interatomic Models [18,19]. It is important to note that several of the above mentioned models [5–7] employ the popular EAM potentials for Fe developed by Mendelev *et al.*

---

[*] sergei.starikov@icams.rub.de

[20,21]. Thus these binary models inherit all advantages as well as disadvantages of these Fe parametrizations (details are discussed in our recent study [3]).

B. Fe-H potentials

To date, several interatomic potentials have been developed to simulate the binary Fe-H system [22–25]. Similarly to many potentials for the Fe-Cr system, the Fe part for most of the Fe-H models is based on one of Mendelev's EAM parametrizations [20,21] complemented by Fe-H and H-H parts. It was found that some of these potentials exhibit a nonphysical clustering of interstitial H atoms dissolved in bcc Fe matrix (see discussion in Supplementary Information of Ref. [24]), which arises due to inadequate description of the H-H interaction [23]. Song and Curtin [24] attempted to correct for this problem by introducing an additional screening function, but this artefact remains if H concentration exceeds 2 at.% (see discussion in Sec. VI E).

III. ADP PARAMETRIZATION FOR THE TERNARY FE-CR-H SYSTEM

During the development of a new ADP potential for the Fe-Cr-H ternary system, we followed the same methodology used for pure iron [3]. The ADP formulation and the Fe parametrization have been presented in detail in our recent publication [3], so here we only briefly present the basic features relevant for the ternary potential construction. This class of potentials has been proposed by Mishin *et al.* [26] as an extension of the widely used EAM formalism. In the ADP model, the total potential energy U for a multicomponent system is given as a sum of five contributions:

$$U = \sum_{i>j} \varphi_{\alpha\beta}(r_{ij}) + \sum_{i} F_\alpha(\overline{\rho}_i) + \frac{1}{2}\sum_{i,k}\left(\mu_i^k\right)^2 + \frac{1}{2}\sum_{i,k,l}\left(\lambda_i^{kl}\right)^2 - \frac{1}{6}\sum_{i}\nu_i^2, \tag{1}$$

where the individual terms are expressed as follows:

$$\overline{\rho_i} = \sum_{j\neq i}\rho_\beta(r_{ij}), \quad \mu_i^k = \sum_{j\neq i} u_{\alpha\beta}(r_{ij})r_{ij}^k,$$
$$\lambda_i^{kl} = \sum_{j\neq i} w_{\alpha\beta}(r_{ij})r_{ij}^k r_{ij}^l, \quad \nu_i = \sum_k \lambda_i^{kk}. \tag{2}$$

The indices i and j enumerate atoms while the indices α and β denote the element types. The superscripts $k, l = 1, 2, 3$ refer to the Cartesian components of vectors and tensors. The $\varphi_{\alpha\beta}(r_{ij})$ term in Eq. (1) represents pair interactions between atoms. The summation is performed over all neighbors j of the atom i (within the cutoff distance r_{cut}, which we set to 6.2 Å). The term $F_\alpha(\overline{\rho}_i)$ is the embedding energy which is a function of the total electron density $\overline{\rho}$. These two terms are similar to those introduced within the classical EAM model. The additional terms μ, λ and ν introduce noncentral interactions through the dipole vectors and quadruple tensors. Due to this functional improvement, ADP models may reach greater accuracy in the description of noncubic structures in comparison with the original EAM formulation. In terms of computational efficiency, the ADP format is only slightly slower than the EAM format.

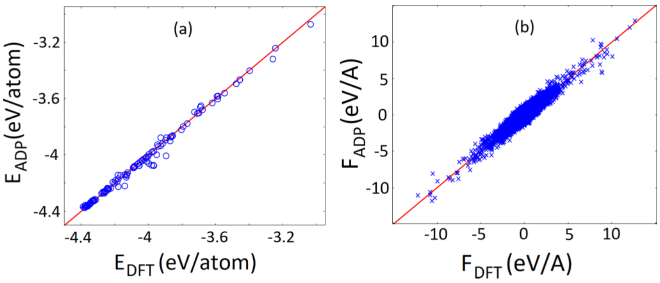

FIG. 1. A comparison of the energy (E) and forces (F) computed with the ADP with respect to the reference DFT data for the same configurations: (a) energy per atom averaged over all atoms in the configuration and (b) force per atom.

The potential functions included in Eq. (1) were determined using the force-matching method [27], which we successfully applied in our previous works [3,28–31]. This method gives a way to construct physically justified interatomic potentials based on the *ab initio* results, without including experimental data in the fitting. The idea is to adjust the interatomic potential functions to optimally reproduce per atom forces (together with total energies and stresses) computed at the *ab initio* level for a fine-tuned set of the reference structures (i.e., configurations) representing the system. In this work, the potential functions were implemented in the form of cubic splines, whose nodes were optimized using a simulated annealing algorithm implemented in the POTFIT code [32,33].

The reference dataset included 131 configurations representing the Fe-Cr-H system. The energy, forces and stresses for each configuration were obtained from DFT computations using the VASP code [34]. A detailed description of 41 configurations containing only iron atoms is given in Ref. [3]. We also added the description of the reference configurations to Ref. [35]. The complete dataset includes various bulk phases (solid, liquid) and crystal defects of Fe, Cr, Fe-Cr, Fe-H, and Fe-Cr-H systems. Each configuration contains about 100–360 atoms, depending on the structure and composition. In the VASP computations, the Brillouin zone was sampled using the 2 × 2 × 2 Monkhorst-Pack $\boldsymbol{k}$-point mesh. The cutoff energy of the plane-wave basis was set to 430 eV. We used spin-polarized calculations with projector augmented wave (PAW) pseudopotentials included in the VASP package and the exchange-correlation functional within the generalized-gradient approximation (GGA) in the form of Perdew-Burke-Ernzerhof.

In total, the reference DFT database included 131 energy values, 444 stress tensor values (6 stress components per configuration with attributed forces), and 53 280 values of the force components. Figure 1 illustrates the quality of the fitting in terms of representation of the reference *ab initio* data. In case of a perfect matching, all points plotted in Figs. 1(a) and 1(b) would be strictly on the diagonal line representing a perfect agreement between the DFT data and the potential results. One can see that most points lie in a close vicinity of the diagonal. The accuracy of the developed model estimated with respect to the reference DFT data is about 245 meV/Å for the forces and 31 meV/atom for the energies. The final potential parametrization in the LAMMPS setfl format can be downloaded from the NIST repository [16,17]. All ADP calculations in this work were performed using the LAMMPS Molecular Dynamics Simulator [36].

The developed potential is aimed to the description of the material in ground magnetic state. In previous paper [3], we discussed in detail the limitation of such approach at the modeling of Fe-based systems. To take into account the magnetic excitation at high temperature, an atomistic model should be combined with spin dynamics approach [37–39].

IV. VALIDATION FOR THE Fe-Cr SYSTEM

In this section, we present a basic validation of the ADP parametrizations for the two elemental metals and their binary system. In the case of pure iron, a comprehensive validation of the ADP potential has already been provided in our original work [3], so only the fundamental properties are repeated here to enable consistent comparisons.

A. Properties of pure iron

In addition to our original validation [3], we use this opportunity to compare the Fe ADP model to two other potentials, namely, a recent artificial neural network (ANN) potential developed by Mori *et al.* [40] and an older EAM potential from Ref. [21]. This EAM parametrization is relevant here, since it was employed in binary potentials for the Fe-Cr system [7] and the Fe-H system [24,25].

Table I contains a summary of basic properties for the body-centred cubic (bcc) phase of Fe (α-Fe). Simulation details for these tests are described in Ref. [3]. It is evident from the table that ANN and ADP models predict the formation and migration energies of simple point defects, i.e., a monovacancy and a self-interstitial (SIA), with the same accuracy. On the other hand, the binding energies of divacancy and di-SIA (denoted as E^b_{divac} and E^b_{disia}) are significantly overestimated by the ANN potential in comparison with DFT results [48]. Apparently, this inaccuracy of the ANN potential results from incompleteness of the training set used for the model development.

In Fig. 2, we compare the energy-volume curves for four competing phases computed by different atomistic models. DFT data are taken from Refs. [49,50]. According to the DFT calculations, the ferromagnetic (FM) state is the most stable magnetic ordering for bcc, A15, and C15 structures. However, for the fcc phase the preferable magnetic ordering depends on volume and changes from the FM state to the antiferromagnetic double-layer (AFMD) state and further to the antiferromagnetic (AFM) and eventually nonmagnetic (NM) state with decreasing volume. Even though the classical models are incapable of distinguishing between the magnetic phases, two basic features of the E-V curves are desired in a classical simulation: (1) an intersection of the bcc and fcc curves under compression, and (2) no intersection of the bcc curve with any other curves under expansion (at least for $12 < V < 14$ Å^3/atom). These features are reproduced by the ADP and ANN models, while the EAM model fails to describe correctly the bcc-fcc energy ordering under both compression and expansion. On the other hand, ANN predicts incorrectly the behavior of A15 and C15 phases. Comparing the results, we can conclude that among the studied models only ADP predicts the E-V curves of the tested structures with a good accuracy and its overall transferability is also superior.

TABLE I. The tested properties of α-Fe: lattice parameter at zero temperature a_0 in angstrom; cohesive energy E_{coh} in eV/atom; elastic constants C_{ij} in GPa; linear thermal expansion α_L in 10^{-5} K^{-1}; the formation/migration energies of vacancy and SIA in eV; and binding energies of divacancy and di-SIA in eV. The last line contains a computational time t_c (in 10^{-6} s/step/atom) for a MD simulation.

	Expt.	DFT	EAM	ANN	ADP
a_0	2.855[a]	2.834[b]	2.855	2.836	2.830
E_{coh}	4.28[c]	—	4.013	6.58	4.376
C_{11}	240[d]	297[b]	243	276	255
C_{12}	136[d]	151[b]	145	175	116
C_{44}	121[d]	105[b]	116	110	113
α_L	1.35[e]	—	0.91	1.1	1.37
E^f_{vac}	—	2.19[f]	1.72	2.2	2.04
E^m_{vac}	—	0.70[g]	0.62	0.85	0.79
E^f_{sia}	—	4.32[f]	3.51	4.36	4.22
E^m_{sia}	0.30 ± 0.02[h]	0.34[f]	0.29	0.19	0.17
E^b_{divac}	—	0.24[i]	0.23	0.63	0.19
E^b_{disia}	—	0.90[i]	0.84	1.45	0.98
t_c	—	—	2	2926	9

[a] Reference [41].
[b] Reference [42].
[c] Reference [43].
[d] Reference [44].
[e] Reference [45].
[f] Reference [46].
[g] Reference [3].
[h] Reference [47].
[i] Reference [48].

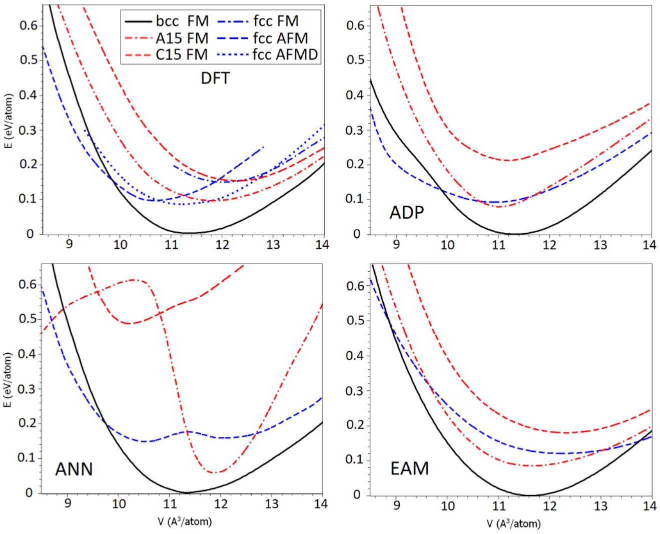

FIG. 2. Energy-volume curves for different Fe phases (bcc, fcc, A15, and C15) described by different atomistic models. DFT data are taken from Refs. [49,50].

TABLE II. The basic properties of bcc Cr simulated with the tested potentials, the units are the same as in Table I. In addition, the melting temperature T_m is given in Kelvin and the surface energies γ_s are given in J/m^2.

	Expt.	DFT	EAM	ADP
a_0	2.878	2.862[a]	2.878	2.835
E_{coh}	4.10	—	3.84	4.09
C_{11}	394[b]	448[a]	411	462
C_{12}	89[b]	62[a]	106	85
C_{44}	104[b]	102[a]	105	112
α_L	0.85[c]	—	1.1	0.91
E^f_{vac}	—	3.00[a] 2.96[d]	2.56	2.48
E^m_{vac}	—	1.1[d]	1.0	1.1
E^f_{sia}	—	6.52[a]	5.53	5.31
T_m	2140±10[e]	—	2610	2210
γ_s^{100}	—	3.98[f] 3.25[g]	2.61	3.59
γ_s^{110}	—	3.51[f]	2.23	3.54
γ_s^{111}	—	4.12[f]	2.71	3.79

[a] Reference [54].
[b] Reference [58].
[c] Reference [59].
[d] Reference [55].
[e] Reference [60].
[f] Reference [56].
[g] Reference [57].

Another advantage of the ADP model is its low computational cost in comparison with the machine learning (ML) interatomic potentials such as ANN or GAP [40,48,51]. The estimated computational times for each model in Table I show that ADP is only 3–4 times slower than EAM while ANN and GAP are several orders of magnitude more expensive. Hence, ADP is suitable for large-scale molecular dynamics (MD) simulations of complex phenomena that require a robust and reliable model.

B. Properties of pure chromium

To date, several classical potentials have been reported for atomistic simulations of chromium-containing alloys [13,52,53]. We validated our ADP parametrization for pure chromium against available DFT data, but we also took into consideration predictions of the EAM potential developed by Olsson *et al.* [13] since this model is employed by several Fe-Cr potentials [7,13]. A summary of the basic properties for bcc Cr from both theoretical calculations and experiments is provided in Table II. The comparison of the ADP and EAM results with the DFT [54–57] and the experimental data [58–60] reveals approximately the same level of accuracy for both potentials. The only exceptions are the melting temperature T_m and the surface energies γ_s predicted by the EAM potential that are noticeably different from the available DFT and the experimental data.

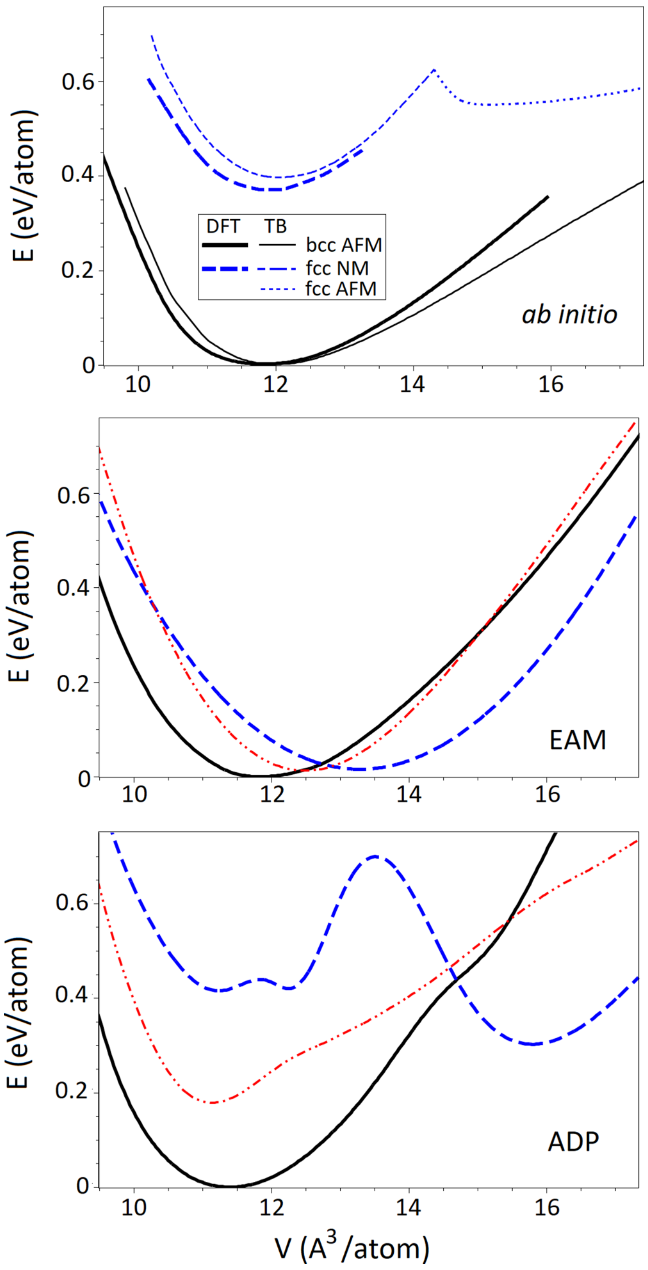

FIG. 3. Energy-volume curves for different Cr phases obtained with different models. The upper panel shows results of DFT [61] and TB [62] calculations for NM and AFM bcc phases. The two lower panels show simulation results for EAM and ADP models, where the bcc phase is shown with the black solid line, fcc with blue dashed line, and A15 with red dash-dotted line.

Calculations of the energy-volume dependencies provide a quick and convenient information about possible structural transformations. Such dependencies, obtained for three different structures (bcc, fcc, and A15), are shown in Fig. 3 together with DFT [61] and tight binding (TB) results [62]. It is interesting to note that for the fcc phase the TB calculation predicts a transition from NM to AFM. Such transformation leads to the occurrence of two local minima on the fcc E-V curve. We see that ADP qualitatively reproduces such a peculiarity and generally describes the energies with a good accuracy. On the other hand, the EAM parametrization for Cr can barely distinguish between the three phases. Moreover, the curves representing different phases intersect near the equilibrium volume, which may lead to nonphysical phase transformations at slight lattice expansion at finite temperature MD simulations or in the vicinity of crystal defects. A similar problem

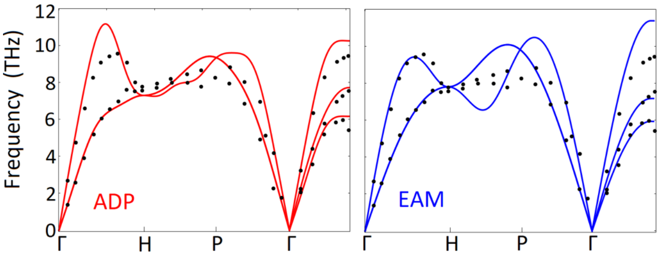

FIG. 4. Phonon dispersion spectra for bcc Cr calculated with two interatomic potentials. The experimental data [64] are depicted by black dots.

was reported for some of the Fe potentials, see Ref. [3] for details.

To assess the stability of both potentials for MD simulations, we computed phonon dispersion spectra by means of the small displacement method as implemented in the PHONOPY software package [63]. Figure 4 shows phonon band structures along high-symmetry directions in the bcc Brillouin zone. Based on the comparison with the experimental data [64], we can conclude that both potentials describe atomic vibrations in bcc Cr well.

The validation confirms that the ADP parametrization provides an adequate description for a number properties of pure Cr. Overall, the predictive ability of the developed potential is similar to that of other classical Cr potentials with a similar degree of complexity in the description of interatomic interactions [52,53].

C. Properties of Fe-Cr alloys

To validate the description of the binary Fe-Cr interactions, we evaluated the mixing enthalpies and the vacancy migration barriers for a number of Fe-Cr alloys with varying compositions. The validation studies were carried out using our ADP model as well as the EAM potential developed by Eich *et al.* [7].

Figure 5(a) illustrates the dependencies of the mixing enthalpy H_{mix} on the Cr concentration in the random alloy. The difference in magnetic properties of iron and chromium atoms leads to the anomalous dependency of H_{mix} on Cr content. At low Cr concentrations, H_{mix} is negative due to the AFM magnetic ordering of Cr atoms that is energetically favorable with respect to the FM state of Fe matrix. However, with increasing Cr concentration this ordering competes with the preferred AFM ordering between neighboring Cr atoms, leading to magnetically frustrated configurations. This results in positive mixing enthalpies for alloys containing more than 7-10 atomic percent of Cr [14,15,65,67,68]. The phase diagram of Fe-Cr alloy also confirms such peculiarity of the concentration dependence of the mixing enthalpy: modeling [68,69] and measurements [70–72] indicate that the limit of Cr solubility in Fe-rich region at low temperature is about 5-8 atomic percent. To test the reproduction of this feature by the classical potentials, we calculated H_{mix} for Fe-Cr alloys. The simulated system contained 3456 atoms with random distribution of the alloying elements. Even though the classical potentials do not contain any explicit description of the magnetic interactions, both of them correctly reproduce the unusual composition dependency of H_{mix}.

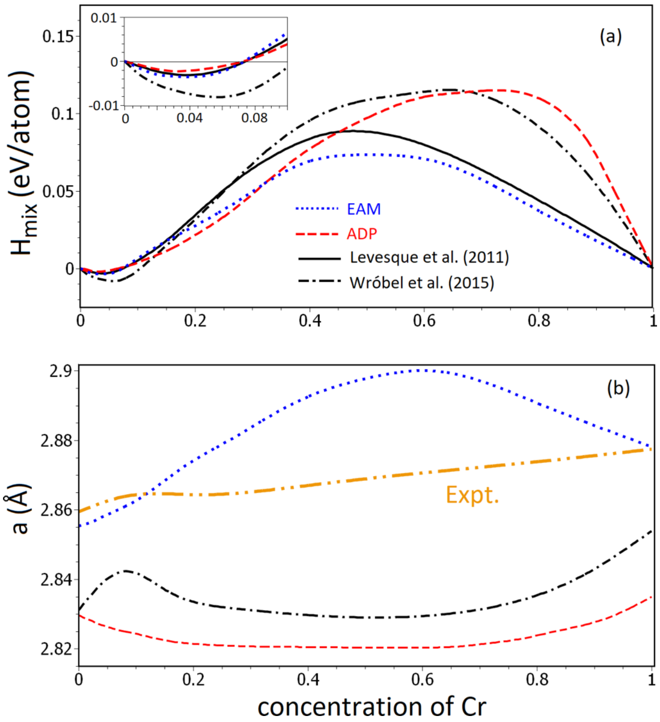

FIG. 5. Variations of the mixing enthalpy (a) and the equilibrium lattice parameter (b) on the Cr content in random Fe-Cr alloys. The DFT data (black lines) are taken from Refs. [15,65] and the experimental data (green dash-dot-dot line) from Ref. [66].

Changes of the equilibrium lattice parameter as a function of composition are shown in Fig. 5(b). Here we notice that according to the experimental data [66] and DFT modeling [65,68] the lattice parameter exhibits a local peak at small Cr concentrations (less than 15 at.%) regardless of the quantitative difference between the absolute values. This phenomenon has been discussed in several works [67,68]. According our tests, the both tested potentials do not reproduce this feature. Nevertheless, the prediction given by ADP agrees rather well with DFT [65] at Cr concentration more than 20 percents. On the other side, the EAM potential shows qualitatively different behavior which differs from both the experimental and DFT results.

It is important to stress that Fe-Cr alloy has no stable intermetallic compounds at low temperature. Hence, the reliable interatomic potential should predict a positive sign of formation enthalpy for any intermetallic structure. To verify this property, we calculated the formation enthalpies and the equilibrium volumes for 14 intermetallic compounds. As the reference data, we used the DFT calculations from OQMD database [73,74]. Figure 6 shows the predictions made with the tested potentials (H_{pot} and V_{pot}) in comparison with the reference DFT values. Results obtained with the potentials are consistent with the reference data, a positive sign of the enthalpies are predicted for all simulated compounds.

The magnitude of vacancy migration barrier depends on the type of migrating atom and the local chemical environment around the vacancy. As an important part of the

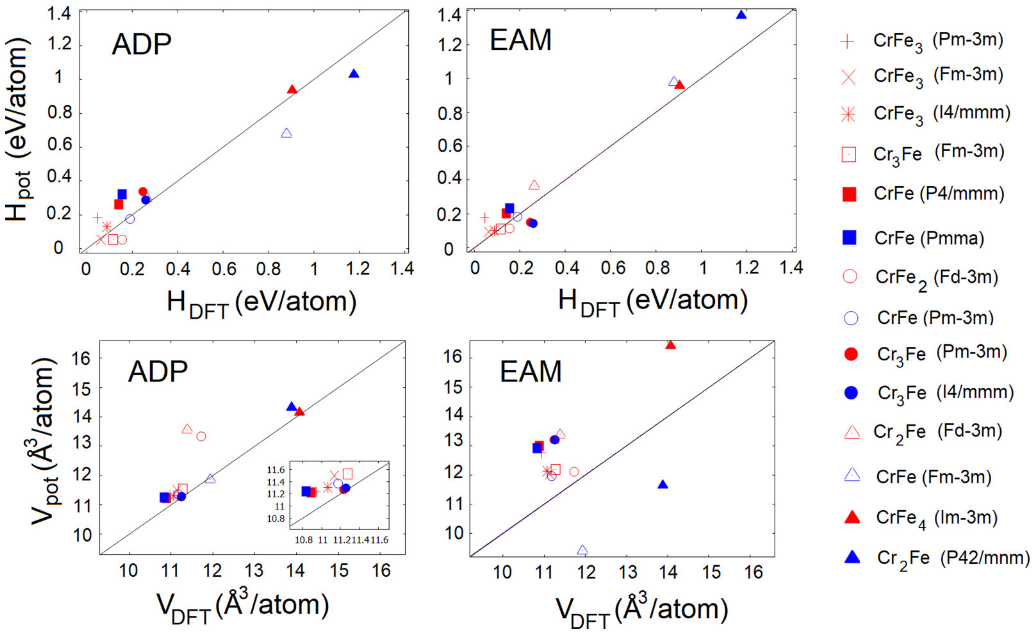

FIG. 6. The formation enthalpies and the equilibrium volumes for 14 intermetallic compounds: the comparison of the interatomic potentials predictions with the reference DFT values from OQMD database.

validation closely related to diffusion, we calculated the migration barrier for a Cr atom moving to a vacancy with different local atomic environments. These calculations were carried out in the spirit of the DFT modeling performed by Costa *et al.* [75]. The migration barriers were calculated using the Nudged elastic band (NEB) method [76]. Table III contains the energy barriers $E^m_{\rm Cr}$ characterizing the vacancy-Cr exchange, and the energy differences ΔE between the final and initial states (i.e., the structures after and before the migration took place). The simulations were performed for three different cases. The first one is a vacancy-Cr exchange in pure bcc iron (i.e., only a single Cr atom exists in the system). The second and the third cases represent migrations of Cr atom taking place in the vicinity of an additional Cr atom. The considered A and B1 environments were taken from the original DFT study by Costa *et al.* [75]. The simulations performed with the classical potentials revealed that $E^m_{\rm Cr}$ and ΔE values depend only slightly on the chemical environment, in contrast to the DFT results. Also, the both tested potentials do not reproduce a tendency to strong space separation of Cr atoms that was obtained by DFT (based on the negative values of ΔE). This discrepancy is likely due to magnetic effects which are not included in the classical models. Nevertheless, both potentials correctly reproduce the basic feature of the migration: $E^m_{\rm Cr}$ is lower than the migration barrier of a vacancy in pure iron (see Table I for comparison).

TABLE III. An exchange barrier between a vacancy and Cr atom. The DFT data are taken from Ref. [75].

	DFT	EAM	ADP
$E^m_{\rm Cr}$ for single Cr	0.57	0.55	0.35
$E^m_{\rm Cr}$ for A environment	0.22	0.62	0.41
$E^m_{\rm Cr}$ for B1 environment	0.31	0.61	0.39
ΔE for A environment	−0.31	−0.09	0.03
ΔE for B1 environment	−0.27	0.02	0.04

V. HYDROGEN IN Fe AND Cr

In this section, we apply the developed potential to evaluate how hydrogen interacts with different crystal defects. Here we report results for a monovacancy, screw dislocation, grain boundaries, and surfaces. Most of the simulations were done for the Fe-H system, but several key cases were also performed for the Cr-H system. In addition, we examined the collective interaction of hydrogen atoms in bcc Fe matrix, which is related to the possibility of iron hydride formation.

We compare our results with those obtained by the EAM model of Song and Curtin [24]. One should keep in mind that this EAM parametrization is a modified version of the potential developed previously by Ramasubramaniam *et al.* [23]. The modification essentially introduced an additional screening function that reduces an excessive nonphysical attraction between H atoms [24]. It should also be noted that there exist several variations both for the original EAM potential [23] and the screening modification [24]. For the calculations performed in this work, we chose to use the original EAM parametrization denoted as "potential B" (aimed mostly at description of bulk properties of the Fe-H system) together with the screening function parameters denoted as "set A." The choice was governed by the comments made in Refs. [23,24].

A. Hydrogen interstitial in perfect crystal

It is known that the bcc lattice has two possible occupation sites for H interstitial: tetrahedral (T) and octahedral (O) [77,78]. According to DFT calculations [23,79,80], the T site should be most favourable for the H interstitial in α-Fe at

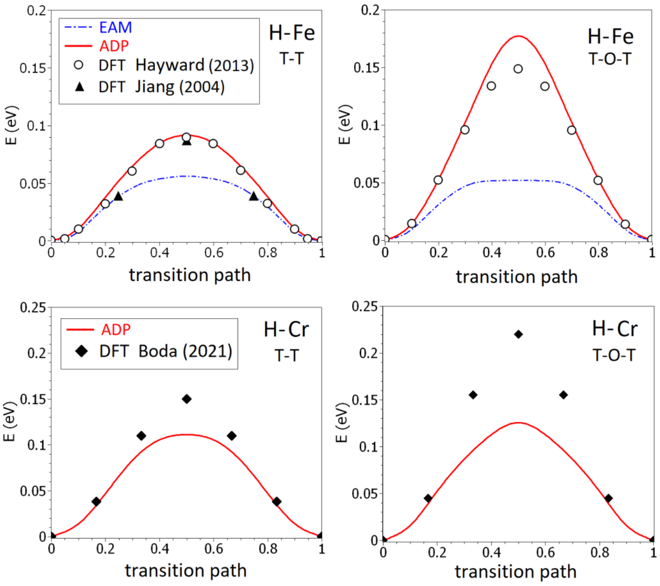

FIG. 7. Migration barriers for a single H atom in bcc Fe (upper panels) and bcc Cr (lower panels). The simulation results obtained with the classical potentials are compared with the available DFT data [79,81,82].

low H concentrations. In our tests, both potentials correctly reproduce this feature. In addition, the ADP model predicts the T site in bcc Cr to be the most stable position of H atom, in agreement with the recent DFT results [81].

H atom can migrate from the given T site either directly to the nearest T site (T-T path along the $\langle 110 \rangle$ direction) or pass through the intermediate O-site (T-O-T path along the $\langle 100 \rangle$ direction). We calculated the migration barriers for both paths using NEB. The simulated structure contained 250 metal atoms and a single H interstitial. In all considered cases, the cell parameters corresponded to zero pressure. The obtained migration barriers are shown in Fig. 7 together with available DFT data [79,81,82].

For H in α-Fe, the migration barriers predicted by ADP agree rather well with the values obtained from the DFT [79,82]. Namely, the T-T and T-O-T migration paths have the energy barriers of about 0.10 and 0.15 eV, respectively. In contrast, the height of the barrier predicted by the EAM potential is almost identical for both migration paths and amounts to only about 0.05 eV. It is worth mentioning that this low value of E_m is due to fitting of the potentials to the zero-point-energy (ZPE) corrected migration barrier [23]. Such ZPE-corrected value correlates better with the measured energy of H migration in α-Fe [83–85]. Our ADP parametrization was fitted to the DFT data without considering the ZPE corrections since its inclusion would disrupt the consistency between energy and forces in the force-matching procedure. In addition, we believe that a proper way to take into account quantum effects necessitates more involved theoretical approaches instead of changing the potential [80,86,87].

The migration barriers for H interstitial in a bcc Cr matrix are described only qualitatively, where the energies for both barriers are underestimated by ADP. Nevertheless, the developed potential correctly reproduces the predicted difference in H migration for the two metals, namely, E_m for the T-T path in Cr is higher than in Fe.

A more general case of H migration under applied stress was also considered in our simulations. Here we present our results showing the influence of different tensile and compressive strains on the magnitude of E_m for the T-T path in Fe. Figure 8 shows the obtained dependencies for both potentials together with our DFT results. All calculations were carried out for computational cells containing identical number of atoms. We performed two types of straining: (i) hydrostatic, where the strain was applied on the system equally in all directions, and (ii) uniaxial, with the strain applied either parallel or perpendicular to the plane containing the migration path. According to the DFT computations, the hydrostatic straining has nearly no effect on the migration barrier. Contrary to this result, the EAM potential predicts a lowering of E_m under compression (negative strain) whereas ADP predicts a slight increase in E_m at the same conditions. In the case of uniaxial strain, DFT and classical models predict mostly the same changes in E_m with the applied strain for both tested deformation directions. By comparing the predictions of both potentials, we can conclude that ADP reproduces the DFT simulation results with better accuracy than EAM.

B. Interaction of H with vacancy

A correct description of H behavior in the vicinity of a vacancy presents another important test. The H binding with the monovacancy has been investigated extensively using DFT [23,79,82,88–90]. All these studies consistently show that a single vacancy in bcc Fe may accumulate up to five H atoms with average binding energies ranging between −0.6 and −0.4 eV. These energies are consistent with experimental measurements [91] that provided values of about −0.63 eV for vacancies containing one to two deuterium atoms and of about −0.45 eV for larger occupations. The negative values correspond here to preferable binding between H (or D) and the vacancy.

In our work, we evaluated the H segregation energy E_s using a supercell containing 250 Fe (or Cr) atoms and a single vacancy. Different numbers of H atoms ($N_H = 1,\ldots,6$) were placed in the vicinity of the vacancy, and the system was relaxed (only atoms positions, no volume changes were made). The initial positions of H atoms near the vacancy were varied to find the arrangement with the lowest energy. For each considered N_H, up to twenty variations in the initial H positions were tested. The segregation energies were calculated as

$$E_s = E(N_H) - E(N_H - 1) - E_H + E_{id},$$

where $E(N_H)$ and $E(N_H - 1)$ are the energies of the simulated systems containing N_H and $(N_H - 1)$ H atoms in the vacancy, E_{id} is the energy of perfect bulk crystal (containing 250 metal atoms), and E_H is the energy of a crystal containing one H atom occupying the T site (i.e., 251 atoms in total). The calculated segregation energies as function of N_H for the minimum energy configurations are plotted in Fig. 9.

The results show that our ADP parametrization for Fe can correctly reproduce the favorable H segregation for up to five H atoms, albeit the segregation energy for the fifth atom is too small (about −0.01 eV). For the EAM model, the maximum

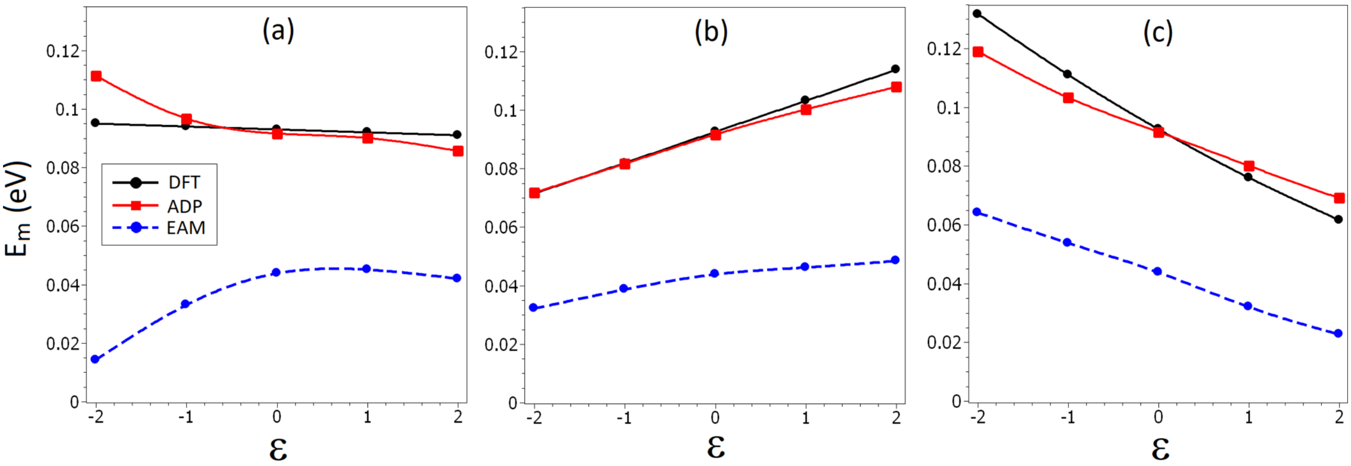

FIG. 8. Calculated migration barrier of H atom in Fe matrix depending on the applied strain. The calculation results for three different conditions are shown: (a) hydrostatic strain; (b) uniaxial strain applied along the plane containing migration path; and (c) uniaxial strain applied perpendicular to the plane containing migration path.

possible number of H atoms near a vacancy is four. It is interesting to note that the favorable H trapping is qualitatively similar in Fe and Cr, but the magnitude of the segregation energies in Cr is about twice as large as in Fe. For Cr, the ADP predictions agree well with the DFT results [81].

Apart from the H segregation, Hayward and Fu [82] investigated in their DFT study also the energy barriers associated with H migration in the vicinity of vacancy in Fe. As a part of our validation, we calculated the same transitions using NEB. A comparison of the obtained energy profiles is shown in Fig. 10. Both ADP and EAM reproduce the energy barriers with approximately the same accuracy. The only difference between the potentials is seen for the last segment of the pathway between the T4 and O2 interstitial sites, where EAM predicts a double-humped energy profile as opposed to ADP and DFT [82].

C. Interaction of H with screw dislocation in Fe

The H trapping at the $\frac{1}{2}\langle 111\rangle$ screw dislocations (S111), which govern the low temperature plasticity in bcc Fe [92–94], has been addressed in several theoretical and experimental studies [95–103]. In a detailed DFT study, Itakura *et al.* [101] identified a number of strong and weak binding sites near the S111 core. They used a simulation cell with the thickness of three Burgers vectors (marked as 3b in the following) to minimize the interactions between H atoms along the dislocation line, and employed the Green's function boundary conditions [104] to investigate a single dislocation in an effectively infinite crystal. To complement this information, we conducted additional DFT calculations using periodic supercells with the thickness of one Burgers vector (marked as 1b in the following) that are commonly used in DFT studies of screw dislocations in bcc metals [105]. Our goal was to examine the influence of boundary conditions and supercell thickness on the H interaction.

A comparison of the DFT segregation energies (marked by black symbols) for different H sites is shown in Fig. 11. For a detailed description of the H sites (E1,...,E9), the reader is referred to the original publication [101]. Interestingly, we found that the effect of supercell thickness and geometry is very small, not exceeding 0.02 eV. The DFT results

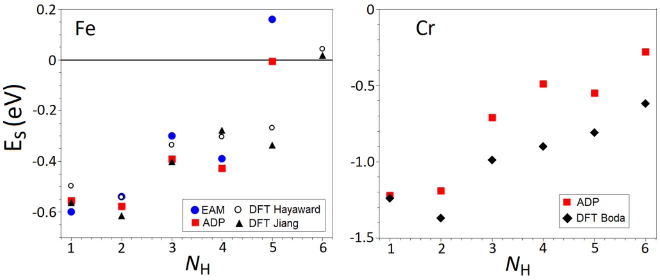

FIG. 9. Calculated segregation energies for H at a mono vacancy in bcc Fe (left) and Cr (right) as a function of the number of segregated H atoms. The different symbols correspond to simulation results obtained with ADP–red squares, EAM–blue circles, DFT [82]–open black circles, DFT [79]–black triangles, and DFT [81]–black diamonds.

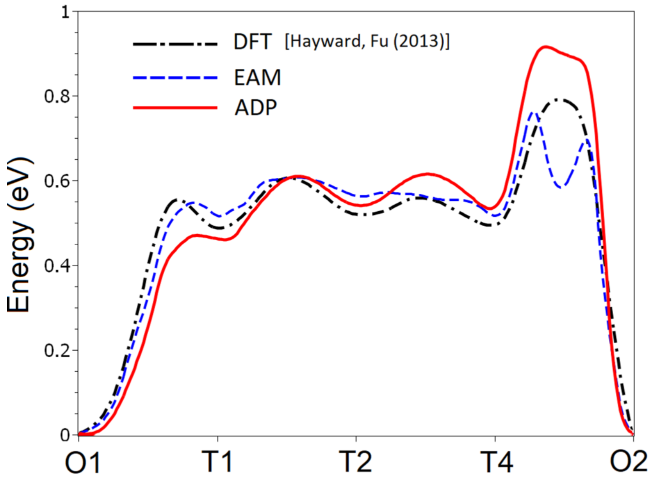

FIG. 10. The energy barriers associated with H migration in the vicinity of vacancy in bcc Fe computed using ADP, EAM, and DFT [82] approaches.

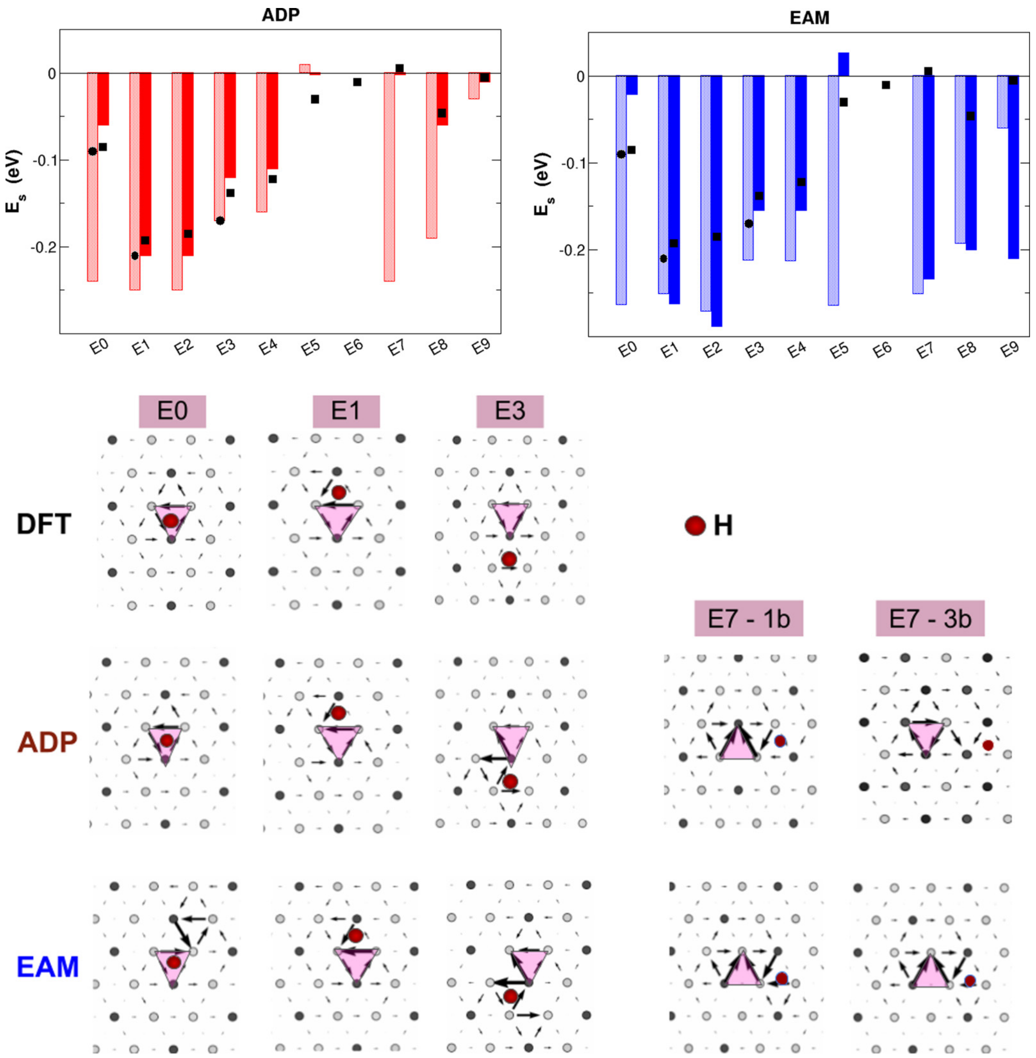

FIG. 11. A comparison of segregation energies for various trap sites around the S111 dislocation in Fe (upper graphs). The light shaded and solid bars correspond to the 1b and 3b cells, respectively. The DFT results are marked by the black circles (1b periodic cell, this work) and black squares (3b nonperiodic cell, Ref. [101]). The lower panels illustrate DD maps (screw component) for several core configurations; the pink triangles mark the position of the core center without segregated H.

consistently show that H prefers the sites next to the dislocation core (E1 and E3) more than the sites in the dislocation center (E0). The differential displacement (DD) plots in Fig. 11 reveal that according to DFT the compact core structure of the screw dislocation remains mostly unaffected by H.

Equivalent calculations were carried out using the ADP and EAM potentials and the calculated segregation energies are depicted as bars (light shaded bars correspond to the 1b cells and solid bars to the 3b cells) in Fig. 11. Both potentials show larger differences between the 1b and 3b cells than DFT, especially for the central E0 site and the more distant weak binding sites. The most significant size effect is observed for the E7 site for ADP and for the E0 and E5 sites for EAM. These large differences can be explained based on the DD maps in Fig. 11. The DD maps from the 1b supercells show in most cases much larger distortions of the cores for ADP and EAM than for DFT. A clear connection between the core structure distortions and the segregation energy is demonstrated for the E7 segregation site in both 1b and 3b supercells (only ADP and EAM are shown). Cores from the 1b cells optimized with both ADP and EAM exhibit significant screw components in the adjacent triangles away from the dislocation center towards the H segregation site. This suggests strong H interactions that give rise to large negative segregation energies. Such a strong core extension does not occur in the 3b cell for ADP whereas it remains for EAM. This difference is reflected by the segregation energies where the EAM values for the 1b and 3b cells are almost the same while for ADP the segregation energy for the 3b cell drops to zero.

The data in Fig. 11 show that the ADP segregation energies for the 3b cells agree very well with the DFT results. Hence, the ADP parametrization can be applied with good confidence in simulations of the interaction between the S111 dislocation and H at low H concentrations. For high H concentration, both potentials show deficiencies in the predicted segregation energies as well as core structures. The marked core distortions are probably related to the underestimation of the S111 Peierls

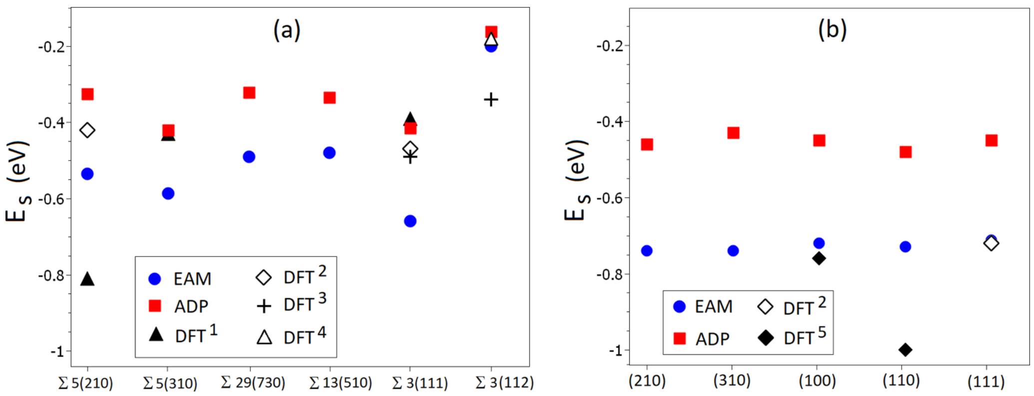

FIG. 12. A comparison of H segregation energies for (a) tilt GBs and (b) free surfaces. In addition to the simulation results with the classical potentials (ADP and EAM), the segregation energies obtained with DFT approach are shown: DFT^1–Ref. [107], DFT^2–Ref. [100], DFT^3–Ref. [108], DFT^4–Ref. [109], and DFT^5–Ref. [23].

barrier by ADP and EAM (see Ref. [3] for details). Especially for EAM, the Peierls barrier has a pronounced double-hump shape with a metastable split core configuration, which is a known artefact of the employed EAM potential for Fe. The EAM results obtained here are consistent with those reported by Wang *et al.* [106]. Investigations of other dislocation types is a subject of a forthcoming study.

D. Interaction of H with planar defects

Planar defects including internal interfaces, grain boundaries (GB), and free surfaces usually present favorable sites for H accumulation. In this work, we considered H segregation at several symmetric tilt GBs and related low-index surfaces. We limit our discussion here to the most favorable segregation sites. More detailed information about the additional segregation sites is provided in Ref. [35].

The calculated segregation energies for six GBs are shown in Fig. 12(a) together with the available DFT data. The EAM potential gives in most cases larger negative segregation energies than ADP, but otherwise the results of both potentials are consistent and show a similar trend. The strongest trapping sites are typically located within a close vicinity of the GB plane [35]. The $\Sigma3(112)$ twin GB shows the weakest trapping. This is consistent with the DFT study of Matsumoto *et al.* [108]. For all remaining GBs, the maximum values of segregation energies range approximately between -0.4 and -0.3 eV for ADP, and -0.7 and -0.5 eV for EAM. The ADP predictions agree well with the available DFT results with the exception of the value -0.81 eV for the $\Sigma5(210)$ GB reported by Mirzaev *et al.* [107]. This discrepancy can be likely attributed to a high-energy metastable GB structure considered in this work. We observed that the presence of H can lead in some cases to local changes in the GB structures [35].

The calculated H segregation energies for free surfaces (FS) are plotted Fig. 12(b). In this work, we considered five different FS orientations. The figure illustrates probably the main disadvantage of the developed ADP, which is a systematic underestimation of the surface segregation energies. According to the DFT results [23,100,107], the magnitude of segregation energies at FSs is about twice as large as that at GBs. The EAM potential agree better here with the DFT results than ADP. Such disadvantage of the ADP potential results from the small number of the such configurations in the training set of the potential.

E. Simulations of iron hydride

According to the DFT calculations [23,110,111], the dissolution energy of H atom in α-Fe from H_2 gas phase is approximately 0.3 eV/H. A positive sign of this energy indicates a poor hydrogen solubility under ambient conditions that coincides with the experimental observations [95]. Also, the DFT calculations [110,112] revealed that the formation energy of some FeH hydrides is extremely small (about 0.01 eV/H). Such energy hierarchy proves that the formation of hydride inclusions in α-Fe may be energetically more stable than randomly dispersed H interstitials. On the other hand, presence of the hydride inclusions has been confirmed experimentally only at very high hydrogen pressures [113–116]. Thus, the question about the kinetics governing the formation of hydride inclusions is open. Here, we verified the potentials in respect to the simulation of iron hydrides properties.

As we mentioned above, the original EAM potential for the Fe-H system [23] was corrected by Song and Curtin [24] to prevent unphysical H-H interactions that led to formation of H clusters in MD simulations when the bulk H concentration C_H exceeded 1 at.%. Such formation of iron hydride inclusions has never been observed experimentally in Fe under ambient conditions and was considered to be an artefact of the potential. In this work, we extended the calculations to considerably larger H concentrations to examine the possible formation of hydride phases in more detail.

Our MD simulations were carried out using a periodic supercell of bcc Fe with dimensions $5.7 \times 5.7 \times 5.7$ nm^3. Initially, H atoms were added randomly at interstitial sites and the system was equilibrated to establish stress-free conditions using the NPT ensemble and $T = 300$ K. Subsequently, the evolution of the system and the positions of H atoms were traced during several nanoseconds.

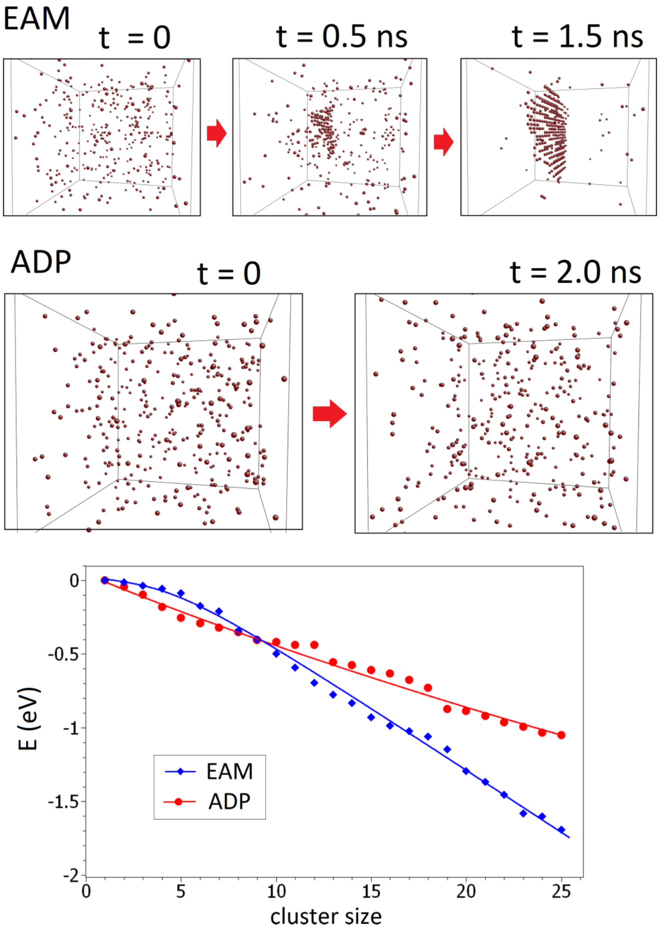

FIG. 13. Results of MD simulations at $T = 300$ K examining the tendency to form H clusters in bcc Fe matrix. The EAM (upper panels) and ADP (middle panels) snapshots (only H atoms are shown) correspond to H concentrations of 2.3 and 7.1 at.%, respectively. The lower graph shows a relative energy of a H cluster with respect to a random H distribution as a function of cluster size.

We found that for C_H higher than 2 at.%, a spontaneous clustering of H atoms still takes place even with the corrected EAM potential. Several snapshots illustrating this process are provided in Fig. 13. Such hydrogen clusterization may be considered as a formation of iron hydride inclusion with the planar structure. Also, we tested another recent EAM parametrization [25] based on the same Fe potential [21] and observed equivalent behavior occurring at the same conditions. In contrast to the situation described above, the distribution of H atoms simulated by the ADP model remained disordered even at $C_H = 7$ at.% (cf. Fig. 13), which agrees with the experimental observations [114,117,118] where no iron hydride inclusions were found in bulk α-Fe up to the hydrogen partial pressure in 3.5 GPa (such pressure corresponds to C_H about 6–8 at.% [114,119]). This modeling revealed that the critical nucleus sizes required to initiate the clusterization are significantly different for the tested potentials.

To obtain a better insight into the stability of H clusters, we simulated a series of cluster configurations in bcc Fe matrix. In these simulations, H atoms were gradually added to the center of the supercell with a size 3.4 × 3.4 × 3.4 nm^3. To find a cluster configuration with the minimal energy, a combination of MD annealing and relaxation of the atomic positions was applied after adding each H atom. The cluster formation energy with respect to the random distribution of H atoms was calculated for each case. The dependencies of the cluster formation energy on the cluster size are shown for the both potentials in Fig. 13. The both potentials predict that the cluster formation energy is negative (hydrogen clusterization is an energy preferable process) and decreases approximately linearly with the increasing cluster size. The decrease is however faster for EAM than for ADP.

TABLE IV. Formation enthalpy (in eV/H) of the planar hydride inclusions with respect to the H atoms dissolved in T sites of bcc Fe matrix. The DFT data are taken from Ref. [110].

	DFT	EAM	ADP
HC_T^{001}	−0.13	−0.06	−0.09
HC_O^{001}	−0.27	−0.24	−0.19

Recent DFT simulations [110] suggest that some planar hydrogen clusters may be formed in α-Fe. The formation enthalpies for two types of infinite planar clusters, one with H atoms occupying the T sites (HC_T^{001}) and the other with H occupying the O sites (HC_O^{001}) on a (001) plane, are compared for DFT, ADP, and EAM in Table IV. The formation enthalpies in our simulations were computed as

$$H_f = \left(\frac{E(N_H) - E_{id}}{N_H}\right) - (E_H - E_{id})$$

where $E(N_H)$ is the energy of the simulated system containing 3456 Fe atoms and N_H H atoms in the planar cluster, E_{id} is the energy of bulk Fe crystal with the same number of Fe atoms, and E_H is the energy of a Fe crystal containing single H atom occupying the T site (3457 atoms in total). All models predict negative formation enthalpies indicating that the formation of such planar hydride clusters from dissolved H atoms is favorable. However, additional aspects related to the kinetics governing the nucleation as well as thermodynamic stability at finite temperatures and internal stress conditions need to be taken into account to fully assess the clustering phenomena.

As a final part of the potentials validation, we calculated the properties of iron hydride with double hexagonal close-packed (dhcp) structure. This structure was observed for FeH in several experiments [113–116]. The basic properties of this FeH hydride are summarized in Table V. Both ADP and EAM give a good agreement with DFT [121]. In addition, the dependencies of the structural parameters on pressure are shown in Fig. 14. For both considered potentials, the calculated lattice parameters (a and c) are slightly different from the

TABLE V. Properties of dhcp FeH phase at zero temperature. DFT data are taken from Ref. [121].

	DFT	EAM	ADP
a (Å)	2.65	2.75	2.63
c/a	3.28	3.27	3.41
B (GPa)	177	172	165

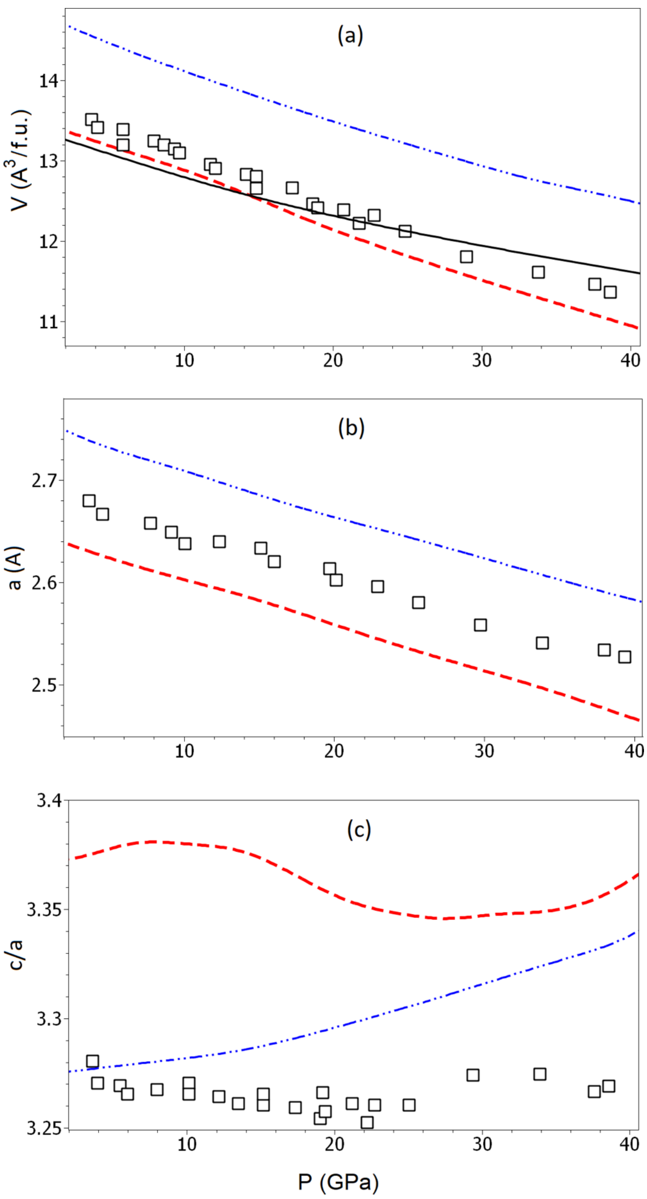

FIG. 14. Properties of dhcp FeH under compression: open squares–experimental data [116]; black solid line–DFT from Ref. [120]; red dashed line–ADP; and blue dash-dot line–EAM.

measured values [116]. Nevertheless, the change in volume with pressure obtained with the ADP model agrees well with the measured curves [116] and DFT data [120].

VI. STUDY OF DIFFUSION PROCESSES

In the previous work [3], we applied the ADP parametrization for Fe to calculate the vacancy diffusion and self-diffusion coefficients (D_{vac} and D_{self}) in both bcc and fcc iron phases. The coefficients obtained for bulk and GB self-diffusion were found to agree well with the experimental measurements. Here we extend the study of diffusion processes by considering the diffusion of interstitial H atoms in the metal matrix. The cases reported here aim to demonstrate the applicability of the developed potential for both pure Fe and Fe-Cr alloys.

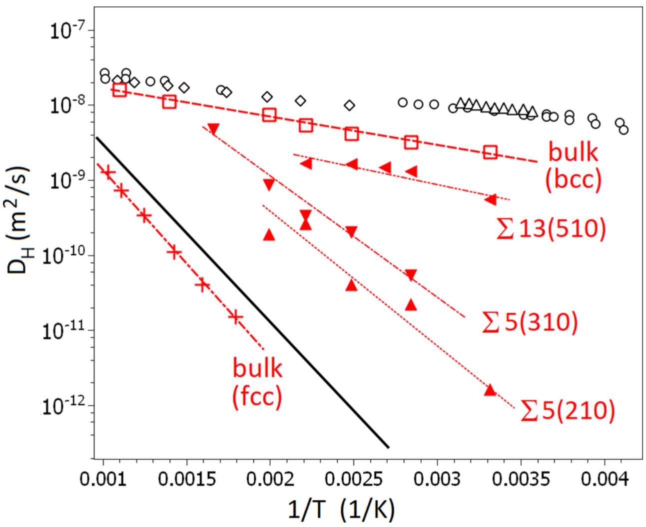

FIG. 15. The temperature dependencies of H diffusion coefficient D_H in different Fe bulk and GB structures. For α-Fe: black hollow symbols–measured coefficients [83–85], red hollow squares–calculated results. For γ-Fe: black solid line is the experimental dependence for this phase [122], red crosses–results of the diffusion simulations. Solid red triangles indicate the calculated diffusion coefficients for different grain boundaries in α-Fe.

Figure 15 provides an overall comparison of H diffusion coefficients in bulk α-Fe and γ-Fe, and along several symmetric tilt GBs in α-Fe. For all these calculations, the diffusion coefficients were estimated from the mean square displacement (MSD) of H atoms during MD simulations with a total simulation time $t = 15$ ns. To trace the H diffusion in the bulk phases, we placed six hydrogen atoms in a periodic simulation cell containing 2000 atoms (α-Fe) or 4000 atoms (γ-Fe) of Fe. The simulated systems were equilibrated at a given temperature (in the range between 300 and 1000 K) and zero pressure. All simulations were done using the NPT ensemble with MD timestep $\Delta t = 0.5$ fs.

The H diffusion along GBs was estimated in a similar manner. We considered three different types of symmetric tilt GBs, namely $\Sigma5(210)$, $\Sigma5(310)$, and $\Sigma13(510)$. To satisfy the periodic boundary conditions, each simulation cell contained two identical GBs. The dimensions of the simulation cells and the simulation setup was the same as in our recent study of GB self-diffusion in Fe [123].

The question about possible differences in H mobility in bulk and along GBs has been raised in several experimental and theoretical works [109,124–126]. Koyama *et al.* [124] carried out *in situ* observations of H permeation in polycrystalline iron specimen by means of silver decoration and detected considerable amounts of H at GBs. However, the observed local H concentration depends on the combination of H segregation and diffusion processes taking place simultaneously, so it does not provide a clear answer about the difference in diffusion coefficients. As discussed above, GBs usually act as strong trapping sites for H which contradicts with the common expectation of the accelerated H diffusion along GBs [125]. From the MD results shown in Fig. 15, it can be seen that H mobility in bulk α-Fe is largest from all considered cases. A slight underestimation in comparison with the measured

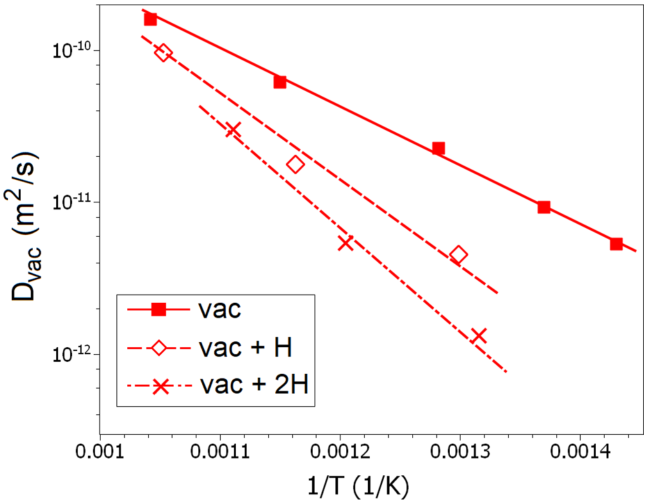

FIG. 16. The calculated diffusion coefficients of vacancy-hydrogen clusters at different temperatures. The simulation results are given for a single vacancy and for a vacancy containing either one or two H atoms.

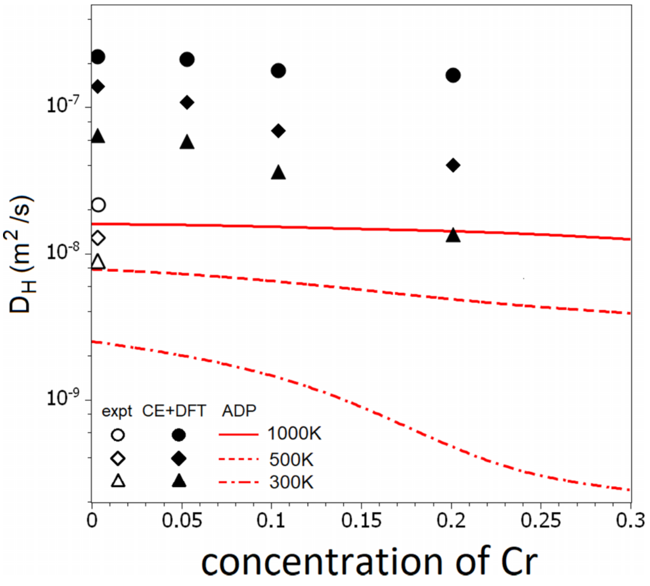

FIG. 17. The impact of Cr concentration on the H diffusion in random Fe-Cr bcc alloy at three different temperatures (see the legend). The open symbols mark experimental values in pure bcc Fe [83–85] while the solid symbols indicate the DFT/CE results [130]. The dependencies calculated in this work are shown by the red lines.

coefficients [83–85,122] is related to the absence of quantum corrections in classical atomistic simulation [80]. In contrast, the H diffusion in fcc γ-Fe is by far the slowest, which is consistent with the diffusion in other related fcc metals such as Ni [80]. The obtained diffusion coefficients for GB diffusion lie in between the two bulk phases so that the mobility of H interstitial is slower inside GBs than in bulk α-Fe but faster than in bulk γ-Fe.

Another phenomenon studied in this work is the diffusion of vacancy-hydrogen clusters. We compared the diffusion of a single vacancy with that of a vacancy with one or two segregated H atoms. The diffusion coefficients of such clusters were traced by the displacement of the vacancy. Figure 16 shows the simulation results for all described cases. It is obvious from this comparison that the presence of H atom(s) in the vacancy significantly reduces its mobility. Interestingly, this outcome is different from that of a recent tight binding simulation study [127], where two H atoms were found to enhance the vacancy diffusion. Since there is no direct experimental data about diffusion of such H-vacancy clusters, this disagreement remains open. However, several experimental observations [128,129] rather indicate a decrease in vacancy mobility in the presence of H.

Finally, we considered an impact of Cr content on H mobility in bcc Fe-Cr solid solution. For this task, six H atoms were placed in simulation cells of varying Fe-Cr compositions containing 6750 metal atoms in total. The H mobility was estimated from the computed MSD, similar to the calculation of D_H in α-Fe. The results of our MD simulations plotted in Fig. 17 show a similar trend as that found in a recent study [130] based on the combination of DFT and cluster expansion (CE). Both theoretical studies predict a decrease in diffusion coefficient as the Cr content in the alloys increases.

VII. CONCLUSION

To create a reliable atomistic model for the description of hydrogen behavior in Fe-Cr alloys, we developed a new angular-dependent interatomic potential. This potential combines high accuracy at the reference data reproduction and low computational cost. Thus, the developed potential gives an opportunity to perform reliable large-scale atomistic simulations of HE-related phenomena. As an example, we carried out a comprehensive study of hydrogen diffusion in pure iron and Fe-Cr alloys. The performed simulation for α-Fe revealed that the interaction of hydrogen with crystal defects (vacancy, GB or Cr alloying atoms) leads in most cases to a marked decrease in the H mobility.

ACKNOWLEDGMENTS

S.S. and R.D. gratefully acknowledge the financial support under the scope of the DFG DR769/8-1 program (MAGIKID project). D.S., T.P., and M.M. gratefully acknowledge the financial support under the scope of the COMET program within the K2 Center ”Computational Material, Process and Product Engineering (IC-MPPE)“ (Project No 859480). This program is supported by the Austrian Federal Ministries for Transport, Innovation and Technology (BMVIT) and for Digital and Economic Affairs (BMDW), represented by the Austrian research funding association (FFG), and the federal states of Styria, Upper Austria and Tyrol. I.G. gratefully acknowledges the financial support by Ministry of Science and Higher Education of the Russian Federation (State Assignment No. 075-01056-22-00). The calculations were carried out on the computer clusters MVS-100K and MVS-10P (Joint Supercomputer Center of RAS) and Vulcan (ICAMS Computing cluster).

[1] M. L. Martin, M. J. Connolly, F. W. DelRio, and A. J. Slifka, Hydrogen embrittlement in ferritic steels, Appl. Phys. Rev. **7**, 041301 (2020).

[2] S. Lynch, Discussion of some recent literature on hydrogen-embrittlement mechanisms: Addressing common misunderstandings, Corrosion Reviews **37**, 377 (2019).

[3] S. Starikov, D. Smirnova, T. Pradhan, Y. Lysogorskiy, H. Chapman, M. Mrovec, and R. Drautz, Angular-dependent interatomic potential for large-scale atomistic simulation of iron: Development and comprehensive comparison with existing interatomic models, Phys. Rev. Materials **5**, 063607 (2021).

[4] B.-J. Lee, J.-H. Shim, and H. M. Park, A semi-empirical atomic potential for the Fe-Cr binary system, Calphad **25**, 527 (2001).

[5] A. Stukowski, B. Sadigh, P. Erhart, and A. Caro, Efficient implementation of the concentration-dependent embedded atom method for molecular-dynamics and monte-carlo simulations, Modell. Simul. Mater. Sci. Eng. **17**, 075005 (2009).

[6] G. Bonny, R. C. Pasianot, D. Terentyev, and L. Malerba, Iron chromium potential to model high-chromium ferritic alloys, Philos. Mag. **91**, 1724 (2011).

[7] S. Eich, D. Beinke, and G. Schmitz, Embedded-atom potential for an accurate thermodynamic description of the iron–chromium system, Comput. Mater. Sci. **104**, 185 (2015).

[8] G. Bonny, D. Terentyev, R. Pasianot, S. Poncé, and A. Bakaev, Interatomic potential to study plasticity in stainless steels: The FeNiCr model alloy, Modell. Simul. Mater. Sci. Eng. **19**, 085008 (2011).

[9] L. K. Béland, A. Tamm, S. Mu, G. D. Samolyuk, Y. N. Osetsky, A. Aabloo, M. Klintenberg, A. Caro, and R. E. Stoller, Accurate classical short-range forces for the study of collision cascades in Fe–Ni–Cr, Comput. Phys. Commun. **219**, 11 (2017).

[10] X. W. Zhou, M. E. Foster, and R. B. Sills, An Fe-Ni-Cr embedded atom method potential for austenitic and ferritic systems, J. Comput. Chem. **39**, 2420 (2018).

[11] M. S. Daw and M. I. Baskes, Embedded-atom method: Derivation and application to impurities, surfaces, and other defects in metals, Phys. Rev. B **29**, 6443 (1984).

[12] B.-J. Lee and M. I. Baskes, Second nearest-neighbor modified embedded-atom-method potential, Phys. Rev. B **62**, 8564 (2000).

[13] P. Olsson, J. Wallenius, C. Domain, K. Nordlund, and L. Malerba, Two-band modeling of α-prime phase formation in Fe-Cr, Phys. Rev. B **72**, 214119 (2005).

[14] A. T. Paxton and M. W. Finnis, Magnetic tight binding and the iron-chromium enthalpy anomaly, Phys. Rev. B **77**, 024428 (2008).

[15] M. Levesque, E. Martínez, C.-C. Fu, M. Nastar, and F. Soisson, Simple concentration-dependent pair interaction model for large-scale simulations of Fe-Cr alloys, Phys. Rev. B **84**, 184205 (2011).

[16] C. A. Becker, F. Tavazza, Z. T. Trautt, and R. A. B. de Macedo, Considerations for choosing and using force fields and interatomic potentials in materials science and engineering, Curr. Opin. Solid State Mater. Sci. **17**, 277 (2013).

[17] L. M. Hale, Z. T. Trautt, and C. A. Becker, Evaluating variability with atomistic simulations: The effect of potential and calculation methodology on the modeling of lattice and elastic constants, Modell. Simul. Mater. Sci. Eng. **26**, 055003 (2018).

[18] E. Tadmor, R. Elliott, J. P. Sethna, R. E. Miller, and C. A. Becker, The potential of atomistic simulations and the knowledgebase of interatomic models, JOM **63**, 17 (2011).

[19] E. B. Tadmor, R. S. Elliott, S. R. Phillpot, and S. B. Sinnott, NSF cyberinfrastructures: A new paradigm for advancing materials simulation, Curr. Opin. Solid State Mater. Sci. **17**, 298 (2013).

[20] M. Mendelev, S. Han, D. Srolovitz, G. Ackland, D. Sun, and M. Asta, Development of new interatomic potentials appropriate for crystalline and liquid iron, Philos. Mag. **83**, 3977 (2003).

[21] G. Ackland, M. Mendelev, D. Srolovitz, S. Han, and A. Barashev, Development of an interatomic potential for phosphorus impurities in α-iron, J. Phys.: Condens. Matter **16**, S2629 (2004).

[22] B.-J. Lee and J.-W. Jang, A modified embedded-atom method interatomic potential for the fe–h system, Acta Mater. **55**, 6779 (2007).

[23] A. Ramasubramaniam, M. Itakura, and E. A. Carter, Interatomic potentials for hydrogen in α–iron based on density functional theory, Phys. Rev. B **79**, 174101 (2009).

[24] J. Song and W. Curtin, Atomic mechanism and prediction of hydrogen embrittlement in iron, Nat. Mater. **12**, 145 (2013).

[25] M. Wen, A new interatomic potential describing Fe-H and hh interactions in bcc iron, Comput. Mater. Sci. **197**, 110640 (2021).

[26] Y. Mishin, M. Mehl, and D. Papaconstantopoulos, Phase stability in the Fe–Ni system: Investigation by first-principles calculations and atomistic simulations, Acta Mater. **53**, 4029 (2005).

[27] F. Ercolessi and J. B. Adams, Interatomic potentials from first-principles calculations: The force-matching method, Europhys. Lett. **26**, 583 (1994).

[28] D. Smirnova, S. Starikov, and A. Vlasova, New interatomic potential for simulation of pure magnesium and magnesium hydrides, Comput. Mater. Sci. **154**, 295 (2018).

[29] S. Starikov, L. Kolotova, A. Y. Kuksin, D. Smirnova, and V. Tseplyaev, Atomistic simulation of cubic and tetragonal phases of U-Mo alloy: Structure and thermodynamic properties, J. Nucl. Mater. **499**, 451 (2018).

[30] S. Starikov, I. Gordeev, Y. Lysogorskiy, L. Kolotova, and S. Makarov, Optimized interatomic potential for study of structure and phase transitions in Si-Au and Si-Al systems, Comput. Mater. Sci. **184**, 109891 (2020).

[31] S. Starikov and D. Smirnova, Optimized interatomic potential for atomistic simulation of Zr-Nb alloy, Comput. Mater. Sci. **197**, 110581 (2021).

[32] P. Brommer and F. Gähler, Potfit: Effective potentials from ab initio data, Modell. Simul. Mater. Sci. Eng. **15**, 295 (2007).

[33] P. Brommer, A. Kiselev, D. Schopf, P. Beck, J. Roth, and H.-R. Trebin, Classical interaction potentials for diverse materials from ab initio data: A review of potfit, Modell. Simul. Mater. Sci. Eng. **23**, 074002 (2015).

[34] G. Kresse and J. Furthmüller, Efficient iterative schemes for ab initio total-energy calculations using a plane-wave basis set, Phys. Rev. B **54**, 11169 (1996).

[35] See Supplemental Material at http://link.aps.org/supplemental/10.1103/PhysRevMaterials.6.043604 for description of the reference structures and the detailed information about H segregation energies for different sites of grain boundaries.

[36] S. Plimpton, Fast parallel algorithms for short-range molecular dynamics, J. Comput. Phys. **117**, 1 (1995).

[37] P.-W. Ma, S. L. Dudarev, and J. S. Wróbel, Dynamic simulation of structural phase transitions in magnetic iron, Phys. Rev. B **96**, 094418 (2017).

[38] J. Tranchida, S. J. Plimpton, P. Thibaudeau, and A. P. Thompson, Massively parallel symplectic algorithm for coupled magnetic spin dynamics and molecular dynamics, J. Comput. Phys. **372**, 406 (2018).

[39] S. Nikolov, J. Tranchida, K. Ramakrishna, M. Lokamani, A. Cangi, and M. Wood, Dissociating the phononic, magnetic and electronic contributions to thermal conductivity: A computational study in alpha-iron, J. Mater. Sci. (2022), doi: 10.1007/s10853-021-06865-3.

[40] H. Mori and T. Ozaki, Neural network atomic potential to investigate the dislocation dynamics in bcc iron, Phys. Rev. Materials **4**, 040601(R) (2020).

[41] Z. S. Basinski, W. Hume-Rothery, and A. Sutton, The lattice expansion of iron, Proc. R. Soc. London A **229**, 459 (1955).

[42] D. Dragoni, D. Ceresoli, and N. Marzari, Thermoelastic properties of α-iron from first-principles, Phys. Rev. B **91**, 104105 (2015).

[43] C. Kittel, *Introduction to Solid State Physics, With Illustrations* (Wiley, New York, 1966).

[44] J. J. Adams, D. Agosta, R. Leisure, and H. Ledbetter, Elastic constants of monocrystal iron from 3 to 500 K, J. Appl. Phys. **100**, 113530 (2006).

[45] Y. Liu, F. Sommer, and E. Mittemeijer, Calibration of the differential dilatometric measurement signal upon heating and cooling; Thermal expansion of pure iron, Thermochim. Acta **413**, 215 (2004).

[46] P.-W. Ma and S. L. Dudarev, Universality of point defect structure in body-centered cubic metals, Phys. Rev. Materials **3**, 013605 (2019).

[47] J. Verdone, W. Chambron, and P. Moser, Magnetic anisotropy induced by self-interstitials in low-temperature electron-irradiated iron, phys. stat. sol. (b) **61**, K41 (1974).

[48] D. Dragoni, T. D. Daff, G. Csányi, and N. Marzari, Achieving DFT accuracy with a machine-learning interatomic potential: Thermomechanics and defects in bcc ferromagnetic iron, Phys. Rev. Materials **2**, 013808 (2018).

[49] L. Dézerald, M.-C. Marinica, L. Ventelon, D. Rodney, and F. Willaime, Stability of self-interstitial clusters with C15 laves phase structure in iron, J. Nucl. Mater. **449**, 219 (2014).

[50] K. Wang, S.-L. Shang, Y. Wang, Z.-K. Liu, and F. Liu, Martensitic transition in Fe via bain path at finite temperatures: A comprehensive first-principles study, Acta Mater. **147**, 261 (2018).

[51] J. Byggmästar, G. Nikoulis, A. Fellman, F. Granberg, F. Djurabekova, and K. Nordlund, Multiscale machine-learning interatomic potentials for ferromagnetic and liquid iron, arXiv:2201.10237.

[52] C. Howells and Y. Mishin, Angular-dependent interatomic potential for the binary Ni–Cr system, Modell. Simul. Mater. Sci. Eng. **26**, 085008 (2018).

[53] V. Maksimenko, A. Lipnitskii, V. Saveliev, I. Nelasov, and A. Kartamyshev, Prediction of the diffusion characteristics of the V-Cr system by molecular dynamics based on n-body interatomic potentials, Comput. Mater. Sci. **198**, 110648 (2021).

[54] P.-W. Ma and S. L. Dudarev, Symmetry-broken self-interstitial defects in chromium, molybdenum, and tungsten, Phys. Rev. Materials **3**, 043606 (2019).

[55] V. Tuli, A. Claisse, L. Messina, and P. Burr, Solubility and vacancy-mediated inter-diffusion in the Zr-Nb-Cr system, J. Nucl. Mater. **548**, 152867 (2021).

[56] L. Vitos, A. Ruban, H. L. Skriver, and J. Kollár, The surface energy of metals, Surf. Sci. **411**, 186 (1998).

[57] T. Ossowski and A. Kiejna, Density functional study of surface properties of chromium, Surf. Sci. **602**, 517 (2008).

[58] S. Palmer and E. Lee, The elastic constants of chromium, The Philosophical Magazine: A Journal of Theoretical Experimental and Applied Physics **24**, 311 (1971).

[59] Y. S. Touloukian, R. K. Kirby, R. E. Taylor, and P. D. Desai, Thermophysical properties of matter - the TPRC data series, Thermal expansion metallic elements and alloys, Report ADA129115, IFI/Plenum, New York (1975).

[60] W. Xiong, M. Selleby, Q. Chen, J. Odqvist, and Y. Du, Phase equilibria and thermodynamic properties in the Fe-Cr system, Crit. Rev. Solid State Mater. Sci. **35**, 125 (2010).

[61] R. Soulairol, C.-C. Fu, and C. Barreteau, Structure and magnetism of bulk fe and cr: From plane waves to lcao methods, J. Phys.: Condens. Matter **22**, 295502 (2010).

[62] R. Soulairol, C. Barreteau, and C.-C. Fu, Interplay between magnetism and energetics in Fe-Cr alloys from a predictive noncollinear magnetic tight-binding model, Phys. Rev. B **94**, 024427 (2016).

[63] A. Togo and I. Tanaka, First principles phonon calculations in materials science, Scr. Mater. **108**, 1 (2015).

[64] W. Shaw and L. Muhlestein, Investigation of the phonon dispersion relations of chromium by inelastic neutron scattering, Phys. Rev. B **4**, 969 (1971).

[65] J. S. Wróbel, D. Nguyen-Manh, M. Y. Lavrentiev, M. Muzyk, and S. L. Dudarev, Phase stability of ternary fcc and bcc Fe-Cr-Ni alloys, Phys. Rev. B **91**, 024108 (2015).

[66] W. B. Pearson, *A Handbook of Lattice Spacings and Structures of Metals and Alloys*, Vols. I and II (Pergamon Press, Oxford, 1958).

[67] P. Olsson, I. A. Abrikosov, and J. Wallenius, Electronic origin of the anomalous stability of Fe-rich bcc Fe-Cr alloys, Phys. Rev. B **73**, 104416 (2006).

[68] A. V. Ruban and V. I. Razumovskiy, First-principles based thermodynamic model of phase equilibria in bcc Fe-Cr alloys, Phys. Rev. B **86**, 174111 (2012).

[69] A. Jacob, E. Povoden-Karadeniz, and E. Kozeschnik, Revised thermodynamic description of the Fe-Cr system based on an improved sublattice model of the σ phase, Calphad **60**, 16 (2018).

[70] S. M. Dubiel and G. Inden, On the miscibility gap in the fe-cr system: A mössbauer study on long term annealed alloys, Int. J. Mater. Res. **78**, 544 (1987).

[71] F. Bergner, A. Ulbricht, and C. Heintze, Estimation of the solubility limit of Cr in Fe at 300 C from small-angle neutron scattering in neutron-irradiated Fe–Cr alloys, Scr. Mater. **61**, 1060 (2009).

[72] S. M. Dubiel and J. Żukrowski, Kinetics of phase separation, border of miscibility gap in Fe–Cr and limit of Cr solubility in iron at 832 K, Mater. Charact. **158**, 109937 (2019).

[73] J. E. Saal, S. Kirklin, M. Aykol, B. Meredig, and C. Wolverton, Materials design and discovery with high-throughput

density functional theory: The open quantum materials database (OQMD), JOM **65**, 1501 (2013).

[74] S. Kirklin, J. E. Saal, B. Meredig, A. Thompson, J. W. Doak, M. Aykol, S. Rühl, and C. Wolverton, The open quantum materials database (OQMD): Assessing the accuracy of dft formation energies, npj Comput. Mater. **1**, 15010 (2015).

[75] D. Costa, G. Adjanor, C. Becquart, P. Olsson, and C. Domain, Vacancy migration energy dependence on local chemical environment in Fe–Cr alloys: A density functional theory study, J. Nucl. Mater. **452**, 425 (2014).

[76] G. Henkelman and H. Jónsson, Improved tangent estimate in the nudged elastic band method for finding minimum energy paths and saddle points, J. Chem. Phys. **113**, 9978 (2000).

[77] J. P. Hirth, Effects of hydrogen on the properties of iron and steel, Metallurgical Transactions A **11**, 861 (1980).

[78] K. Kiuchi and R. McLellan, The solubility and diffusivity of hydrogen in well-annealed and deformed iron, in *Perspectives in Hydrogen in Metals* (Elsevier, 1986), pp. 29–52.

[79] D. E. Jiang and E. A. Carter, Diffusion of interstitial hydrogen into and through bcc Fe from first principles, Phys. Rev. B **70**, 064102 (2004).

[80] D. Di Stefano, M. Mrovec, and C. Elsässer, First-principles investigation of quantum mechanical effects on the diffusion of hydrogen in iron and nickel, Phys. Rev. B **92**, 224301 (2015).

[81] A. Boda, S. Bajania, S. M. Ali, K. Shenoy, and S. Mohan, Chemisorption, diffusion and permeation of hydrogen isotopes in bcc bulk Cr and Cr (100) surface: First-principles dft simulations, J. Nucl. Mater. **543**, 152538 (2021).

[82] E. Hayward and C.-C. Fu, Interplay between hydrogen and vacancies in α-fe, Phys. Rev. B **87**, 174103 (2013).

[83] W. Bryan and B. Dodge, Diffusivity of hydrogen in pure iron, AIChE J. **9**, 223 (1963).

[84] Y. Hayashi, H. Hagi, and A. Tahara, Diffusion coefficients of hydrogen and deuterium in iron determined by permeation with gas, ion and electrochemical charging, Zeitschrift für Physikalische Chemie **164**, 815 (1989).

[85] H. Hagi, Diffusion coefficient of hydrogen in iron without trapping by dislocations and impurities, Mater. Trans., JIM **35**, 112 (1994).

[86] H. Kimizuka, H. Mori, and S. Ogata, Effect of temperature on fast hydrogen diffusion in iron: A path-integral quantum dynamics approach, Phys. Rev. B **83**, 094110 (2011).

[87] B. Cheng, A. T. Paxton, and M. Ceriotti, Hydrogen Diffusion and Trapping in α-Iron: The Role of Quantum and Anharmonic Fluctuations, Phys. Rev. Lett. **120**, 225901 (2018).

[88] Y. Tateyama and T. Ohno, Stability and clusterization of hydrogen-vacancy complexes in $\alpha - \mathrm{Fe}$: An ab initio study, Phys. Rev. B **67**, 174105 (2003).

[89] E. Hayward, B. Beeler, and C. Deo, Multiple hydrogen trapping at monovacancies, Philos. Mag. Lett. **92**, 217 (2012).

[90] A. A. Mirzoev, D. A. Mirzaev, and A. V. Verkhovykh, Hydrogen–vacancy interactions in ferromagnetic and paramagnetic bcc iron: Ab initio calculations, Physica status solidi (b) **252**, 1966 (2015).

[91] F. Besenbacher, S. Myers, P. Nordlander, and J. Norskov, Multiple hydrogen occupancy of vacancies in Fe, J. Appl. Phys. **61**, 1788 (1987).

[92] L. Ventelon, F. Willaime, E. Clouet, and D. Rodney, Ab initio investigation of the peierls potential of screw dislocations in bcc Fe and W, Acta Mater. **61**, 3973 (2013).

[93] Z. Chen, M. Mrovec, and P. Gumbsch, Atomistic aspects of screw dislocation behavior in α-iron and the derivation of microscopic yield criterion, Modell. Simul. Mater. Sci. Eng. **21**, 055023 (2013).

[94] D. Weygand, M. Mrovec, T. Hochrainer, and P. Gumbsch, Multiscale simulation of plasticity in bcc metals, Annu. Rev. Mater. Res. **45**, 369 (2015).

[95] C. Hwang and I.M. Bernstein, Dislocation transport of hydrogen in iron single crystal, Acta Metallurgica **34**, 1001 (1986).

[96] W. Y. Choo and J. Y. Lee, Thermal analysis of trapped hydrogen in pure iron, Metallurgical Transactions A **13**, 135 (1982).

[97] Y. Zhao and G. Lu, QM/MM study of dislocation-hydrogen/helium interactions in α-Fe, Modell. Simul. Mater. Sci. Eng. **19**, 065004 (2011).

[98] R. Gibala, W. A. Counts, and C. Wolverton, The hydrogen cold work peak in bcc iron: Revisited, with first principles calculations and implications for hydrogen embrittlement, Materials Research **21**, e20170868 (2018).

[99] G. Rao, Y. Yagodzinskyy, Z. Que, P. Spatig, and H. Seifert, Study on hydrogen embrittlement and dynamic strain ageing on low-alloy reactor pressure vessel steels, J. Nucl. Mater. **556**, 153161 (2021).

[100] A. S. Kholtobina, R. Pippan, L. Romaner, D. Scheiber, W. Ecker, and V. I. Razumovskiy, Hydrogen trapping in bcc iron, Materials **13**, 2288 (2020).

[101] M. Itakura, H. Kaburaki, M. Yamaguchi, and T. Okita, The effect of hydrogen atoms on the screw dislocation mobility in bcc iron: A first-principles study, Acta Mater. **61**, 6857 (2013).

[102] Y.-S. Chen, D. Haley, S. S. A. Gerstl, A. J. London, F. Sweeney, R. A. Wepf, W. M. Rainforth, P. A. J. Bagot, and M. P. Moody, Direct observation of individual hydrogen atoms at trapping sites in a ferritic steel, Science **355**, 1196 (2017).

[103] Y.-S. Chen, H. Lu, J. Liang, A. Rosenthal, H. Liu, G. Sneddon, I. McCarroll, Z. Zhao, W. Li, A. Guo, and J. M. Cairney, Observation of hydrogen trapping at dislocations, grain boundaries, and precipitates, Science **367**, 171 (2020).

[104] S. Rao, C. Hernandez, J. P. Simmons, T. A. Parthasarathy, and C. Woodward, Green's function boundary conditions in two-dimensional and three-dimensional atomistic simulations of dislocations, Philosophical Magazine A **77**, 231 (1998).

[105] L. Ventelon and F. Willaime, Core structure and peierls potential of screw dislocations in α-Fe from first principles: Cluster versus dipole approaches, J. Computer-Aided Mater. Design **14**, 85 (2007).

[106] S. Wang, N. Hashimoto, and S. Ohnuki, Hydrogen-induced change in core structures of {110}[111] edge and {110}[111] screw dislocations in iron, Sci. Rep. **3**, 2760 (2013).

[107] D. Mirzaev, A. Mirzoev, K. Y. Okishev, and A. Verkhovykh, Ab initio modelling of the interaction of h interstitials with grain boundaries in bcc fe, Mol. Phys. **114**, 1502 (2016).

[108] R. Matsumoto, M. Riku, S. Taketomi, and N. Miyazaki, Hydrogen-grain boundary interaction in Fe, Fe-C, and Fe-N systems, Progress in Nuclear Science and Technology **2** (2011).

[109] Y. A. Du, L. Ismer, J. Rogal, T. Hickel, J. Neugebauer, and R. Drautz, First-principles study on the interaction of H

interstitials with grain boundaries in α- and γ-Fe, Phys. Rev. B **84**, 144121 (2011).

[110] J. Hou, X.-S. Kong, C. Liu, and J. Song, Hydrogen clustering in bcc metals: Atomic origin and strong stress anisotropy, Acta Mater. **201**, 23 (2020).

[111] C. Elsässer, J. Zhu, S. G. Louie, M. Fahnle, and C. T. Chan, Ab initiostudy of iron and iron hydride: I. cohesion, magnetism and electronic structure of cubic Fe and FeH, J. Phys.: Condens. Matter **10**, 5081 (1998).

[112] C. M. Pépin, A. Dewaele, G. Geneste, P. Loubeyre, and M. Mezouar, New Iron Hydrides under High Pressure, Phys. Rev. Lett. **113**, 265504 (2014).

[113] V. Antonov, I. Belash, V. Degtyareva, E. Ponyatovskii, and V. Shiryaev, Obtaining iron hydride under high hydrogen pressure, Soviet Physics Doklady **25**, 490 (1980).

[114] J. Badding, R. Hemley, and H. Mao, High-pressure chemistry of hydrogen in metals: In situ study of iron hydride, Science **253**, 421 (1991).

[115] V. Antonov, K. Cornell, V. Fedotov, A. Kolesnikov, E. Ponyatovsky, V. Shiryaev, and H. Wipf, Neutron diffraction investigation of the dhcp and hcp iron hydrides and deuterides, J. Alloys Compd. **264**, 214 (1998).

[116] N. Hirao, T. Kondo, E. Ohtani, K. Takemura, and T. Kikegawa, Compression of iron hydride to 80 GPa and hydrogen in the earth's inner core, Geophys. Res. Lett. **31**, L06616 (2004).

[117] A. Machida, H. Saitoh, T. Hattori, A. Sano-Furukawa, K.-i. Funakoshi, T. Sato, S.-i. Orimo, and K. Aoki, Hexagonal close-packed iron hydride behind the conventional phase diagram, Sci. Rep. **9**, 12290 (2019).

[118] M. Mohtadi-Bonab and H. Ghesmati-Kucheki, Important factors on the failure of pipeline steels with focus on hydrogen induced cracks and improvement of their resistance, Met. Mater. Int. **25**, 1109 (2019).

[119] Y. Fukai, S. Yokota, and J. Yanagawa, The phase diagram and superabundant vacancy formation in co–h alloys, J. Alloys Compd. **407**, 16 (2006).

[120] H. Gomi, Y. Fei, and T. Yoshino, The effects of ferromagnetism and interstitial hydrogen on the equation of states of hcp and dhcp FeH_x: Implications for the earth's inner core age, American Mineralogist: Journal of Earth and Planetary Materials **103**, 1271 (2018).

[121] T. Tsumuraya, Y. Matsuura, T. Shishidou, and T. Oguchi, First-principles study on the structural and magnetic properties of iron hydride, J. Phys. Soc. Jpn. **81**, 064707 (2012).

[122] H. Mehrer, *Diffusion in Solid Metals and Alloys* (Springer, Berlin, 1990).

[123] S. Starikov, M. Mrovec, and R. Drautz, Study of grain boundary self-diffusion in iron with different atomistic models, Acta Mater. **188**, 560 (2020).

[124] M. Koyama, D. Yamasaki, T. Nagashima, C. C. Tasan, and K. Tsuzaki, In situ observations of silver-decoration evolution under hydrogen permeation: Effects of grain boundary misorientation on hydrogen flux in pure iron, Scr. Mater. **129**, 48 (2017).

[125] V. P. Ramunni, M. I. Pascuet, N. Castin, and A. M. Rivas, The influence of grain size on the hydrogen diffusion in bcc fe, Comput. Mater. Sci. **188**, 110146 (2021).

[126] X.-Y. Zhou, J.-H. Zhu, and H.-H. Wu, Molecular dynamics studies of the grain-size dependent hydrogen diffusion coefficient of nanograined fe, International Journal of Hydrogen Energy **46**, 5842 (2021).

[127] S. Echeverri Restrepo, H. Lambert, and A. T. Paxton, Effect of hydrogen on vacancy diffusion, Phys. Rev. Materials **4**, 113601 (2020).

[128] Y. Sugiyama, N. Kurihara, Y. Matsumoto, and K. Takai, The effects of interstitial hydrogen and carbon atoms and aging temperature on annihilation behavior of hydrogen-enhanced strain-induced vacancies in iron, Scr. Mater. **202**, 114031 (2021).

[129] L. Chiari, A. Nozaki, K. Koizumi, and M. Fujinami, Strain-rate dependence of hydrogen-induced defects in pure α-iron by positron annihilation lifetime spectroscopy, Materials Science and Engineering: A **800**, 140281 (2021).

[130] A. J. Samin, D. A. Andersson, E. F. Holby, and B. P. Uberuaga, First-principles localized cluster expansion study of the kinetics of hydrogen diffusion in homogeneous and heterogeneous Fe-Cr alloys, Phys. Rev. B **99**, 014110 (2019).